Optimal Tuning of Fractional Order PI for a Multi-DG Microgrid using the Starfish Optimization

HAIDY M. ZAKARIA, BESHOY A. AZIZ, ABDELNASER NAFEH, WALEED A. SALEM
Electrical Engineering Department,
Benha Faculty of Engineering, Benha University,
Qalubia,
EGYPT

Abstract: - Nowadays, the smart microgrid is a promising solution to overcome the issues of depleting fossil fuel, climate change, global warming and environmental pollution. A microgrid depends on the installation of renewable and distributed generation sources beside the local loads to minimize the cost of power transmission and high reliability against sudden faults. Among the various renewable energy micro-sources (REMSs) utilized in distributed generation (DG) systems, photovoltaic (PV) technology has gained significant traction due to its modularity, declining costs, and environmental benefits. This paper presents a modified architecture for an AC microgrid that includes six master units (MUs) powered by PV cells. Unlike conventional PI controllers, the proposed Fractional Order Proportional-Integral (FOPI) controllers feature an additional tunable parameter, which increases the complexity of the controller design. To address this, Star Fish optimization techniques are utilized and compared for selecting the optimal parameters of the FOPI controller. The optimization process focuses on enhancing power quality and improving both dynamic and steady-state performance by fine-tuning the HC controller parameters. Multiple objective error functions are used and evaluated to minimize the total harmonic distortion of the grid's output current. The effectiveness of the proposed FOPI controller is verified in MATLAB/Simulink, considering permissible variations in inverter output active and reactive powers, as well as under conditions of grid voltage distortion.

Key-Words: - AC Microgrid, PV, Fractional Order Proportional-Integral, distributed generation, Star Fish, HC controller.

Received: April 14, 2026. Revised: June 13, 2026. Accepted: July 23, 2026. Published: November 5, 2026.

1 Introduction

Currently, the integration of renewable energy micro sources (REMSs) into distributed generation (DG) systems within the utility power grid is rapidly increasing. DG systems based on REMSs such as fuel cells, tidal, hydro, biomass power systems, PV systems, and wind energy conversion systems (WECS) are being widely adopted in distributed power networks to supply clean and sustainable energy, [1]. These DG units interface micro-sources with electrical loads using either power electronic converters or synchronous generators. They offer numerous benefits, including enhanced reliability and protection against sudden faults. Additionally, they promote better local use of renewable energy resources, reduce environmental pollution and greenhouse gas emissions, increase energy efficiency, and lower both transmission line costs and losses, [2]. As such, they serve as a valuable support system for the main power grid. To ensure the effective integration of multiple DG units into the grid as a microgrid, advanced control strategies are essential to minimize operational uncertainties and enhance performance, [3]. Microgrids can operate in two modes:
(1) Grid-connected mode, allowing energy exchange with the main grid [4]; and
(2) Standalone mode, supplying power to local loads during grid outages [5].

The rapid advancement in power electronic converter technologies has facilitated the seamless integration of REMSs, such as PV panels and wind turbines, as primary DG units within micro-grids. However, due to the intermittent and unpredictable characteristics of REMSs, significant power fluctuations may occur, potentially degrading power quality, [6]. To address this issue, energy storage systems (ESSs) are essential, as they enhance both controllability and operational flexibility in micro-grids, [7]. Effective control strategies are critical to ensuring coordinated operation between ESSs, REMSs, and connected loads. A key goal of these coordination strategies is to mitigate power

imbalances between generation and demand, thereby enhancing the reliability and stability of micro-grids, [8].

In micro-grids with multiple DG units, control strategies must go beyond simple regulation tasks and include features such as equitable power sharing among units, [9]. Numerous communication-based control techniques have been explored in the literature, including master-slave configurations without a central controller [10], with a central controller [11], and auto-master-slave schemes [12]. Other notable approaches are the instantaneous average current sharing method [13], peak-value current sharing [14], circular chain control [15], angle droop control [16], and distributed control, [17]. While these methods offer good stability and accurate current distribution, their dependence on communication networks compromises system flexibility, reliability, and redundancy.

The main objective of this paper is to face the micro-grid challenges mentioned above by using FOPI controllers. These controllers have a series of advantages over conventional PI controllers. They enhance the performance of dynamical systems. Furthermore, they reduce the sensitivity to parameters and gain variability. Moreover, they improve gain and phase margins and increase bandwidth. Additionally, they have a robust performance with respect to high frequency noise, [18]. Usually, FOPI controllers have an extra adjustable parameter than the conventional PI controllers. This parameter makes the controller design to be more complex.

2 System Configuration

This paper presents the simulation of a coordinated two-layer hierarchical control strategy applied to the proposed microgrid topology. The design incorporates multiple DG units, with the configuration illustrated by MATLAB in Figure 1 comprising six master units (MUs) to improve system redundancy during islanded operation. Under normal conditions, both active and reactive power are evenly distributed among the six MUs to prevent overloading any individual unit. Additionally, the parameters of the secondary control layer, based on FOPI controllers, are optimized using the Star Fish Optimization (SFO) algorithm to improve the micro-grid's dynamic and steady-state voltage and frequency performance, The source of Figure 1 is MATLAB program simulation.

2.1 Modeling of the PV Array

The mathematical modeling of a PV array is based on the modeling of the PV module. The equivalent circuit of a PV module is the same as the equivalent circuit of a PV array, shown Figure 2, but the number of series (N_{ser}) and parallel (N_{par}) modules must be taken into consideration in case of the PV array. The current model of a PV module can be expressed as [19]:

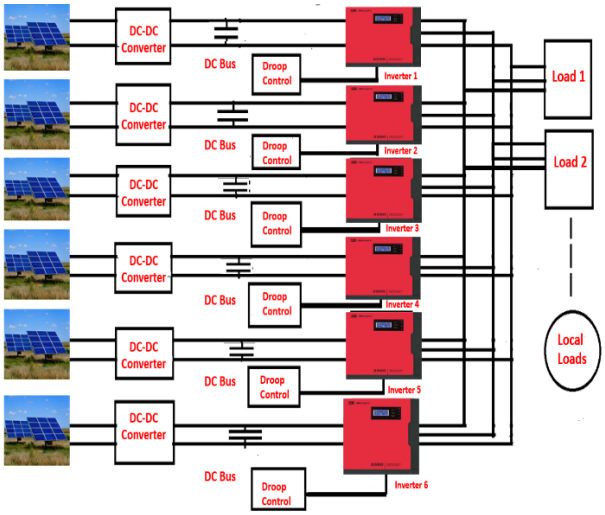


Fig. 1: System proposed architecture of AC microgrid simulation by MATLAB/SIMULINK.

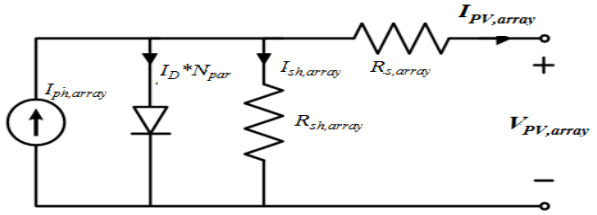


Fig. 2: Equivalent circuit of a PV solar array
Source: created by the authors

$$I_{PV} = I_{ph} - I_o \left[\exp\left(\frac{V_{PV} + I_{PV} R_s}{a N_s V_t} \right) - 1 \right] - \frac{V_{PV} + I_{PV} R_s}{R_{sh}} \quad (1)$$

where,

V_t : the junction thermal voltage and is given by kT/q, V
q : the electron charge, 1.609*10-19 C
k: Boltzmann constant, 1.38*10-23 J/K
T: the temperature of the PN junction, K
V_{PV}: the terminal voltage of the PV cell, V
I_{ph} the photo-generated current by the incident light, A
I_{PV} the output current of the PV cell, A
I_o: reverse saturation or leakage current of the diode, A
a: diode quality factor (ideality factor),
N_s: Number of series cells.

R_s,R_{sh}: Series and shunt cell resistance respectively. The power of a PV module can be obtained from:

$$P_{PV} = V_{PV} I_{PV}$$
$$= V_{PV}\left[I_{ph} - I_o\left[\exp\left(\frac{V_{PV} + I_{PV} R_s}{a N_s V_t} \right) - 1 \right] - \frac{V_{PV} + I_{PV} R_s}{R_{sh}} \right] \quad (2)$$

In our simulation, the type of module is used SPR-305E-WHT-D. Each array consist of 25 modules in parallel and 12 modules in series. The power of array at MPP is 142 Kw at insolation 1000 W/m2. Figure 3 shows the voltage, current and power characteristics of PV array. Other data are in Appendix Table A1.

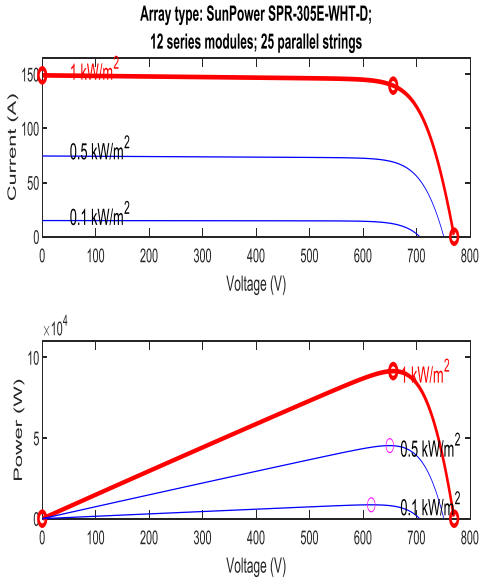


Fig. 3: PV array characteristics
Source: created by the authors

2.2 Modeling of Boost Converter

The output of PV array is fluctuating in nature hence boost converter is required to get MPP DC voltage. Diagram of DC-DC converter consisting of IGBT switch, inductor, diode, and shunt capacitor is as shown in Figure 4. The value of inductance; capacitance and duty cycle can be calculated, [20]:

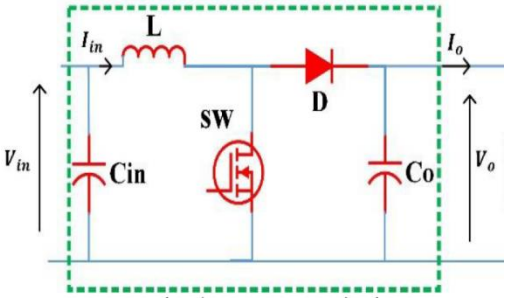


Fig. 4: Schematic diagram of boost converter
Source: created by the authors

$$D=(V_{out}- V_{in})/V_{out} \quad (3)$$

$$\boldsymbol{L} = \frac{\boldsymbol{V_{PVmin} D_{max}}}{\boldsymbol{2\Delta I_{PV} f_{sw}}} \quad (4)$$

$$\boldsymbol{D_{max}} = \frac{\boldsymbol{V_{dc}+V_D}}{\boldsymbol{V_{PVmin}+V_{dc}+V_D}} \quad (5)$$

where, D is duty cycle , V_{in} & V_{out} are DC/DC converter input and output voltage, V_{PVmin} represents the minimum voltage generated by PV panels, Δi_{PV} represents the input current ripple, f SW represent the switching frequency, I_{dc} represents the dc link current, ΔV_{dc} represents the output voltage ripple, and D_{max} represents the maximum duty ratio, [21].

2.3 Control of the MPPT Boost Converter

The control of the boost converter which connected with the PV array is based on the P & O to extract the available MP from the PV array. The input variable is the summation of incremental conductance and the change in the incremental conductance of the PV array as shown in Figure 5.

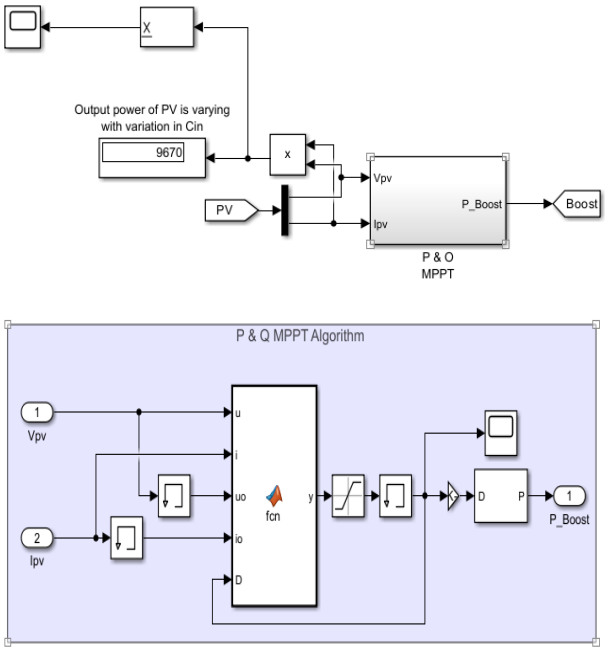


Fig. 5: Implementation of the MPPT Boost converter with Control P & O
Source: created by the authors

2.4 AC Inverter with Filter

The inverter module proposed here contains a push pull DC/DC converter, which provides a DC link voltage. The second stage is a full bridge three phase inverter with FOPI control analog as shown in Figure 6, in Table 1 is shown the microgrid parameters and optimal coefficients of hc controllers to use in simulation system.

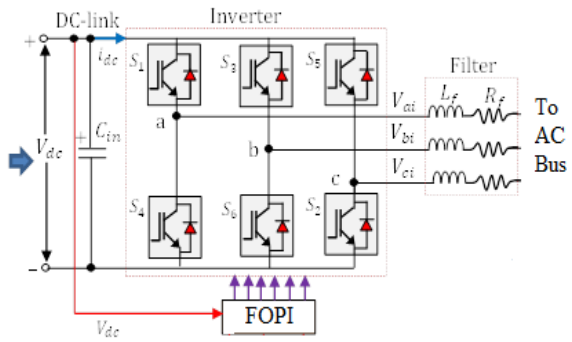


Fig. 6: Inverter with control
Source: created by the authors

Table 1. Proposed microgrid parameters and optimal coefficients of hc controllers

Parameter	Symbol	Value
DC Bus		
DC Capacitor	C_{dc}	3*680e-6 Farad
Sampling Time	T_S	5e-6 sec
Universal Bridge		
Snubber Resistance	R_S	1e5 Ω
Snubber Capacitance	C_S	inf
Internal Resistance	R_{on}	1e-3 Ω
L-Filter		
Resistance	R_F	0.1Ω
Inductance	L_F	1.35e-3 H
C-Filter		
Capacitance	C_F	50e-6 Farad
Coupling Inductor		
Resistance	R_C	0.03 Ω
Inductance	L_C	0.35e-3 H
Droop Control coefficients		
Frequency Droop	D_p	9.4e-5 rad/s/w
Voltage Droop	D_Q	1.3e-3 V/Var
Voltage FOPI Controller coefficients		
Proportional Gain	K_{ppv}	0.1
Integral Gain	K_{ipv}	420
Current FOPI Controller coefficients		
Proportional Gain	K_{ppi}	15
Integral Gain	K_{ipi}	20000
Feed Forward Gain	μ	0.75
Cuttoff Frequency of virtual impedance high pass filter	ω_{cH}	70 rad/sec
Inductance of filter	X_{Lv}	1.35e-3 H
Secondary Control System		
Proportional Gain for Voltage Control	K_{psv}	1.035447
Integral Gain for Voltage Control	K_{isv}	98.08913
Proportional Gain for Frequency Control	$K_{ps\omega}$	0.083242
Integral Gain for Frequency Control	$K_{is\omega}$	11.83408

Source: created by the authors

2.5 Fractional-Order PI Controller (FOPI)

A traditional PI controller uses a proportional gain (K_p) and an integral gain (K_i). A FOPI controller adds fractional-order operators to the integral term (and sometimes the proportional term), providing more flexibility to tune the controller's response.
A standard Proportional-Integral (PI) controller uses integer-order integration (order 1). The Fractional-Order PI (PI^{λ}) controller generalizes this by introducing a non-integer fractional order $\lambda>0$ for the integral term, providing an extra degree of freedom for tuning dynamic responses.

Continuous-Time Domain Model
The continuous-time input-output differential equation of a PI^{λ} controller is:

$$u(t)=K_p\, e(t)+K_i\, D_t^{-\lambda} e(t) \quad (6)$$

where:

- u (t) is the controller output (control signal).
- e (t)= r (t) – y (t) is the error signal between reference input r (t) and system output y (t).
- K_p is the proportional gain.
- K_i is the integral gain.
- $D_t^{-\lambda}$ represents the fractional integration operator of order λ with respect to time t.

Taking the Laplace transform of u(t) assuming zero initial conditions yields the transfer function C(s):

$$C(s)=K_p+K_i/s^{\lambda} = K_p + K_i\, s^{-\lambda} \quad (7)$$

- When λ=1, it reduces to the classical integer-order PI controller (K_p+K_i/s).
- Fractional orders are typically approximated in realization using numerical discretization methods such as the Oustaloup recursive approximation filter.

3 System Simulation

The system consists of six station. Each station is about of PV array and power 142 Kw, DC link, inverter, and filter. All the power of stations are in one of AC bus. This bus supplies eight different loads. The value of loads are Load 1 (14 Kw, 9 KVAR), Load 2 (16 Kw, 6 KVAR), Load 3 (15 Kw, 8 KVAR), Load 4 (12 Kw, 10 KVAR), Load 5 (12 Kw, 8 KVAR), Load 6 (2 Kw, 1 KVAR), Load 7 (5 Kw, 3 KVAR), and Load 8 (14 Kw, 8 KVAR). The system is shown in Figure 7. While, the signal of insulation and temperature are shown in Figure 8. More than 30 alterations were made to achieve optimal system performance.

The output voltage and current of boost converter are shown in Figure 9. The voltage and

current under P & Q control for get MPPT. The output power for big scale is shown in Figure 10. While, Figure 11 is shown the frequency under active and reactive powers control for MPPT

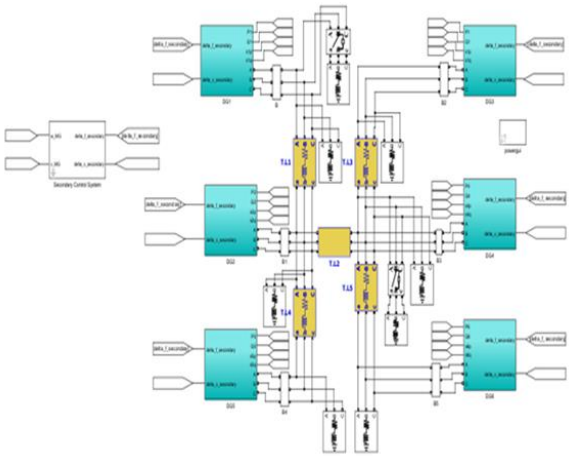


Fig. 7: The simulation of the system
Source: created by the authors

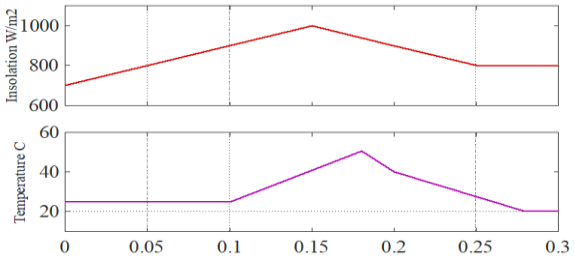


Fig. 8: The signal input of temperature and Insolation to PV array
Source: created by the authors

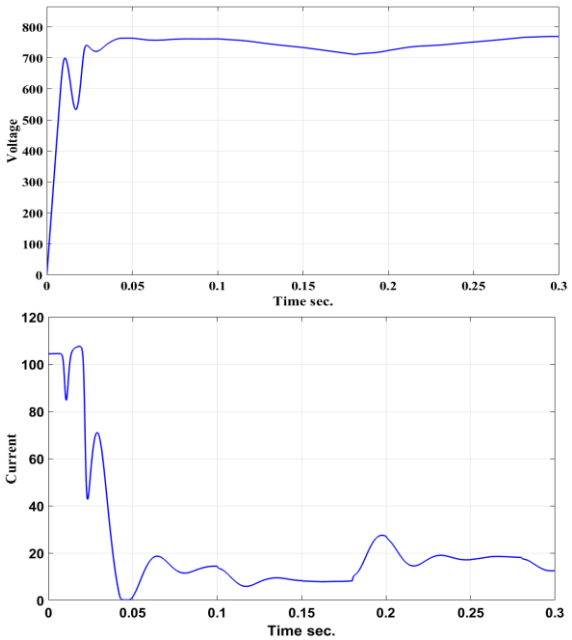


Fig. 9: Voltage and current under P & Q control for MPPT
Source: created by the authors

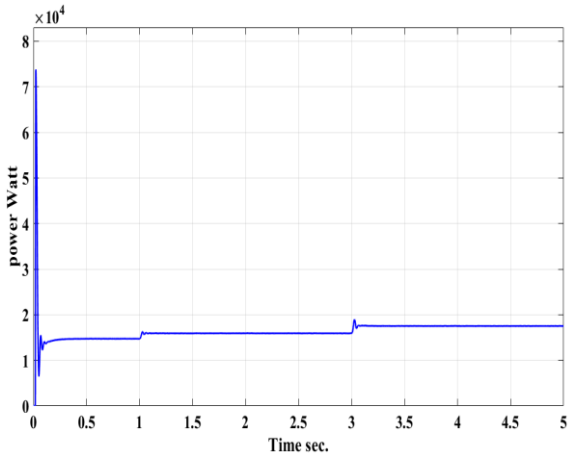


Fig. 10: output power at MPPT for one array
Source: created by the authors

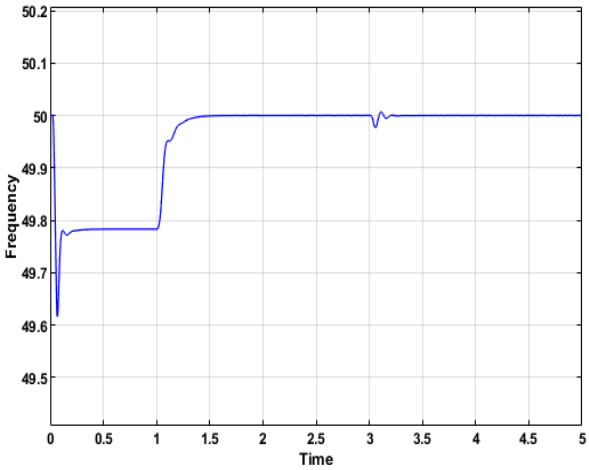


Fig. 11: Frequency under P & Q control for MPPT
Source: created by the authors

3.1 Compare the Results for Inverter and Different Load between PI and FOPI

The three-phase voltage of the load are shown in Figure 12. In Figure 13, the output active and reactive power are present for PI and FOPI. Table 2 and Table 3 are the results of comparison between PI and FOPI for active and reactive powers from simulation.

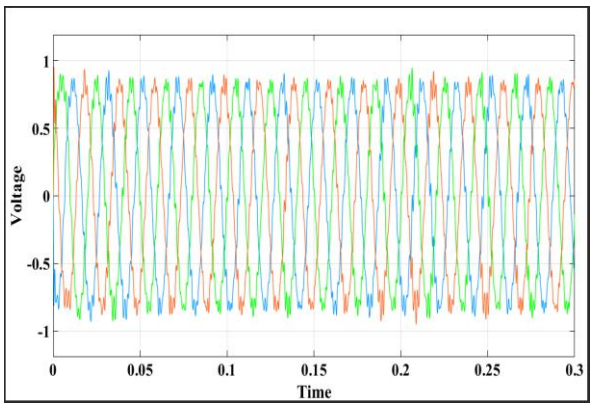
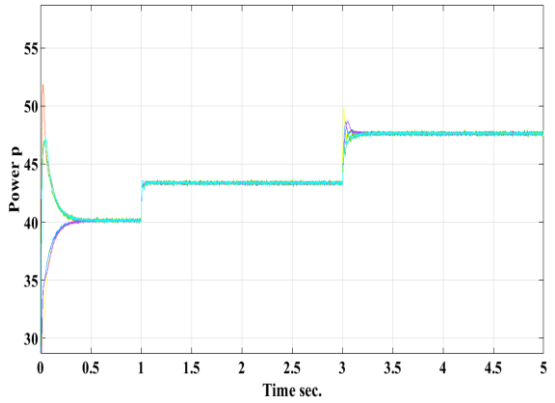
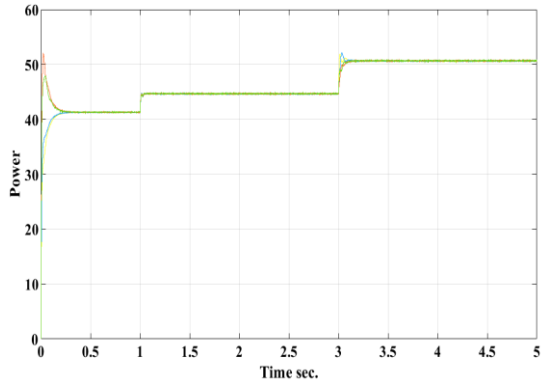


Fig. 12: 3 phases voltage for one load
Source: created by the authors

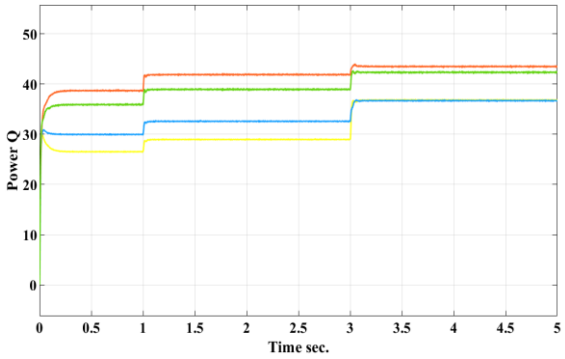


For PI

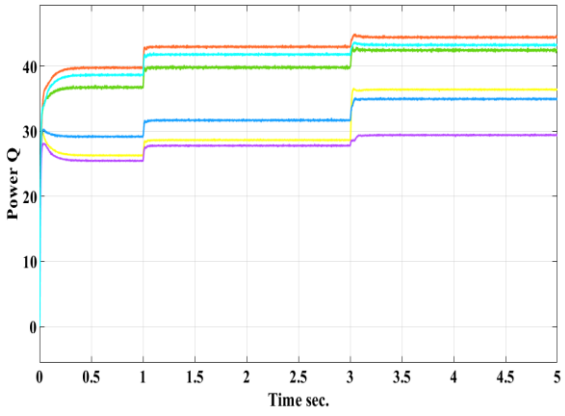


For FOPI

Active power.



For PI



For FOPI

B- Reactive power

Fig. 13: the active and reactive power for different load

Source: created by the authors

Table 2. Results of active power from simulation

Aspect	FOPI Controller	PI Controller
Rise Time	0.15sec	0.25sec
Overshoot	2.03%	4.115%
Settling Time	0.21sec	0.64sec
Steady-State Error	2.14%	5.26%

Source: created by the authors

Table 3. Results of Reactive power from simulation

Aspect	FOPI Controller	PI Controller
Rise Time	0.215sec	0.220sec
Overshoot	0%	0%
Settling Time	0.35sec	0.41sec
Steady-State Error	0%	0%

Source: created by the authors

From the result, the FOPI control is small overshoot, smoother oscillations, settles faster, frequency remains stable with less deviation, and better disturbance rejection. While, the PI control is Work with fixed integral action and more overshoot or slower recovery. From the results, FOPI clearly outperforms PI in frequency stability, disturbance rejection, and settling time.

4 Star Fish Algorithm

The Starfish Optimization Algorithm (SFOA) is a recently developed bio-inspired metaheuristic technique that emulates the natural behavior of starfish to solve global optimization problems [22]. The algorithm operates through three fundamental stages: initialization, exploration, and exploitation. During the initialization stage, the initial positions of all starfish are generated by randomly assigning values to each design variable within its predefined bounds, as described by Equation 6.

$$Z = \begin{bmatrix} z_{11} & z_{12} & z_{1D} \\ z_{21} & z_{22} & z_{2D} \\ z_{N1} & z_{N2} & z_{ND} \end{bmatrix}_{N \times D} \quad (8)$$

Here, **Z** represents the initial positions of the entire starfish population, where **N** denotes the population size and **D** indicates the number of design variables of the optimization problem. Each element $Z_{i,j}$ corresponds to the position of the *i*-th starfish in the *j*-th dimension of the search space. Is calculated using the equation 7.

$$Z_{i,j} = l_j + r\left(u_j - l_j\right),\ \ i = 1,2,\dots,N,\quad j = 1,2,\dots,D \tag{9}$$

In this context $r \in [0, 1]$ represents a uniformly distributed random number, while l_j , $u_j$denote the lower and upper limits of the j-th design variable, respectively. After initializing the positions, the fitness of each starfish is computed by evaluating the objective function, and the corresponding results are recorded in a fitness vector.

$$F = \begin{bmatrix} F(Z_1) \\ F(Z_2) \\ \vdots \\ F(Z_N) \end{bmatrix}_{N\times 1} \tag{10}$$

During the exploration phase, a hybrid search mechanism is applied to simulate the way a starfish uses its five arms, each equipped with sensory capability, to locate food. Depending on the dimensionality of the optimization problem, two different search strategies are adopted: a five-dimensional search pattern and a unidimensional search pattern. When the number of design variables exceeds five (D > 5), the five-dimensional search strategy is employed.

In this case, the movement of each starfish is guided by the best solution found so far and is updated according to equation 9.

$$\begin{cases} X_{i,p}^{T} = Z_{T}^{i,p} + \varphi_1\left(Z_{best.p}^{T} - Z_{i,p}^{T}\right)cos\delta, & r \le 0.5 \\ X_{i,p}^{T} = Z_{T}^{i,p} - \varphi_1\left(Z_{best.p}^{T} - Z_{i,p}^{T}\right)sin\delta, & r > 0.5 \end{cases} \tag{11}$$

Here, the parameters φ_1 and δ are determined using Equation 10 and Equation 11, respectively.

$$\varphi_1 = (2r - 1)\pi \tag{12}$$

$$\delta = \frac{\pi}{2} \cdot \frac{I}{I_{max}} \tag{13}$$

If the updated position violates the allowable limits, the boundaries of the design variables are enforced using Equation 12.

$$Z_{T+1}^{i,p} = \begin{cases} X_{i,P,}^{T} & l_T^{b,p} \le X_{i,p}^{T} \le u_T^{b,p} \\ Z_{i,P,}^{T} & otherwise \end{cases} \tag{14}$$

When the number of design variables satisfies $D \le 5$, a one-dimensional search strategy is adopted. Under this condition, the position of each starfish is updated according to Equation 13.

$$X_{i,q}^{T} = E_I Z_{T}^{i,p} + B_1\left(Z_{Tk_1,p}^{T} - Z_{i,p}^{T}\right) + B_2\left(Z_{Tk_2,p}^{T} - Z_{i,p}^{T}\right) \tag{15}$$

In this case, B_1, B_2 are random coefficients bounded within the interval [−1, 1] while the energy of the starfish, denoted as E_I , is defined according to Equation 14.

$$E_I = \frac{I_{max} - I}{I_{max}}\ COS\delta \tag{16}$$

If an updated position violates the allowable limits, the boundaries of the design variables are enforced using Equation 7. The exploitation phase consists of two main processes: preying and regeneration. In this stage, a parallel bidirectional search strategy is applied, where the algorithm first computes five distances between the best solution found so far and the remaining starfish, as defined by Equation 15.

$$d_{max} = \left(Z_{best}^{T} - Z_{m_p}^{T}\right),\qquad max = 1,\dots,5 \tag{17}$$

In this context, m_p refers to the five starfish selected at random from the population. Subsequently, two of the previously computed distances are randomly chosen as reference values, and the position of each starfish is then updated according to Equation 16.

$$X_i^T = Z_i^T + r_1 d_{max1} + r_2 d_{max2} \tag{18}$$

Here, r_1 and r_2 are random numbers uniformly distributed in the interval [0, 1], while d_{max1}, d_{max2} denote the five distances computed between the global best solution and the other starfish. Following this step, the regeneration phase is activated when $i = N$, during which the position of the starfish is renewed according to Equation 17.

$$X_i^T = \exp\left(\frac{-I \times N}{I_{max}}\right) Z_i^T \tag{19}$$

After the position update, the algorithm verifies whether the new solution exceeds the permitted limits. If any design variable falls outside its allowable range, the boundary constraints are enforced using Equation 18.

$$Z_i^{T+1} = \begin{cases} X_i^T & l_b \le X_i^T \le u_b \\ l_b & X_i^T < l_b \\ u_b & X_i^T > u_b \end{cases} \tag{20}$$

Figure 14 is shown the flowchart of SFOA control. Table 4 is shown the optimal parameters where obtained by the proposed design guidelines for PR voltage and current controllers with their

HCS. While, Table 5 is the dynamic behaviors of proposed optimal secondary controller

Table 4. The optimal parameters where obtained by the proposed design guidelines for PR voltage and current controllers with their HCS

Algorithm	Objective error function	Parameters of secondary				Fitness function value
		Frequency controller		Voltage controller		
		$K_{ps\omega}$	$K_{is\omega}$	K_{psv}	K_{isv}	
conventional	-	0.04	25	0.01	188	-
Star Fish	IAE	0.0141	14.460	0.0721	153.30	984.34
	ITAE	0.0399	12.997	0.0364	129.79	280.58
PSO	IAE	0.0246	17.581	0.1592	178.28	1180.64
	ITAE	0.0566	19.141	0.1407	148.41	325.96
GWO	IAE	0.0527	18.761	0.4512	168.51	1088.26
	ITAE	0.0550	16.723	0.6962	172.25	377.190

Source: created by the authors

Table 5. Dynamic behaviors of proposed optimal secondary controller

Algorithm	Objective error function	Studied condition			
		Microgrid initiation			
		Max. over-shoot (%)		Settling time(s)	
		frequency	voltage	frequency	voltage
conventional	-	0.2865	1.66737	0.8343	0.25992
Star Fish	IAE	0.116246	0.8842	0.070923	0.0738
	ITAE	0.121285	0.4261	0.066192	0.0515
PSO	IAE	0.151010	1.4700	0.224590	0.1202
	ITAE	0.193176	1.0746	0.364815	0.1247
GWO	IAE	0.164860	1.0053	0.317113	0.1069
	ITAE	0.149197	0.7911	0.202080	0.1001

Source: created by the authors

5 Conclusion

In this paper, the modified architecture for an AC microgrid that includes six master units (MUs) powered by PV cells is presented. The system consists of PV array connected with a DC/DC boost converter, inverter with FOPI control, and AC loads. The microgrid of system is comparison between the PI and FOPI control. The effectiveness of the proposed FOPI controller was verified in MATLAB/Simulink, considering permissible variations in inverter output active and reactive powers, as well as under conditions of grid voltage distortion. The optimization process focuses on enhancing power quality and improving both dynamic and steady-state performance by fine-tuning the HC controller parameters. The FOPI controller demonstrated clearly smoother and faster dynamic response than the PI controller.

Declaration of Generative AI and AI-assisted Technologies in the Writing Process

During the preparation of this work, the author(s) utilized artificial intelligence (AI) technologies solely for the purpose of linguistic refinement and grammatical correction. Following the application of these tools, the author(s) comprehensively reviewed, verified, and edited the resulting text. The author(s) maintain full accountability and responsibility for the accuracy, integrity, and final content of the publication.

References:

[1] H. Hu, N. Xie, D. Fang, and X. Zhang, "The role of renewable energy consumption and commercial services trade in carbon dioxide reduction: Evidence from 25 developing countries", *Appl. Energy*, vol. 211, Feb. 2018, pp. 1229-1244.

[2] M. S. shirband, J. Salehi, and F. S. Gazijahani, "Decentralized trading of plug-in electric vehicle aggregation agents for optimal energy management of smart renewable penetrated microgrids with the aim of CO_2 emission reduction", *Journal Cleaner Prod*., vol. 200, Nov. 2018, pp. 622-640.

[3] C. Wang, J. Yan, C. Marnay, N. Djilali, E. Dahlquist, J. Wu, and H. Jia, "Distributed energy and microgrids (DEM)", *Appl. Energy*, vol. 210, Jan. 2018, pp. 685-689.

[4] J. M. Guerrero, J. C. Vasquez, J. Matas, L. García de Vicuna, and M. Castilla, "Hierarchical control of droop-controlled AC and DC microgrids A general approach toward standardization", *IEEE Trans. Ind. Electron.*, Vol. 58, No. 1, Jan. 2011, pp. 158-172.

[5] S. Riverso, M. Tucci,J. C. Vasquez, J. M. Guerrero, and G. Ferrari-Trecate, "Stabilizing plug-and-play regulators and secondary coordinated control for AC islanded microgrids with bus-connected topology", *Appl. Energy*, Vol. 210, Jan. 2018, pp. 914-924.

[6] X. Feng, A. Shekhar, F. Yang, R. E. Hebner, and P. Bauer, "Comparison of hierarchical control and distributed control for microgrid", *Electr. Power Compon. System*, Vol. 45, No. 10, June 2017, pp. 1043-1056.

[7] J. Wu, C. Zhang, and Z. Chen, "An online method for lithium-ion battery remaining useful life estimation using importance sampling and neural networks", *Appl. Energy*, Vol. 173, Jul. 2016, pp. 134-140.

[8] J. Hu, Y. Xu, K. W. Cheng, and J. M. Guerrero, "A model predictive control strategy of PV-battery microgrid under variable power

generations and load conditions", *Appl. Energy*, Vol. 221, Jul. 2018, pp. 195-203.

[9] M. Kim and A. Kwasinski, "Decentralized hierarchical control of active power distribution nodes", *IEEE Trans. Energy Convers.*, Vol. 29, No. 4, Dec. 2014, pp. 934-943.

[10] T. L. Vandoorn, J. D. M. De Kooning, B. Meersman, and L. Vandevelde, "Review of primary control strategies for islanded microgrids with power electronic interfaces", *Renew. Sustain. Energy Rev.*, Vol. 19, Mar. 2013, pp. 613-628.

[11] W.-C. Lee, T.-K. Lee, S.-H. Lee, K.-H. Kim, D.-S. Hyun, and I.-Y. Suh, "Amaster and slave control strategy for parallel operation of three-phase UPS systems with different ratings", *Proc. 19th Annu. IEEE Appl. Power Electron Conf. Expo.* (APEC), Anaheim, CA, USA, 2004, pp. 456-462.

[12] Y. Pei, G. Jiang, X. Yang, and Z. Wang, "Auto-master-slave control technique of parallel inverters in distributed AC power systems and UPS", Proc. *IEEE 35th Annu. Power Electron. Spec. Conf., Aachen, Germany*, Jun. 2004, pp. 2050-2053.

[13] X. Sun, Y. S. Lee, and D. Xu, "Modeling, analysis, and implementation of parallel multi-inverter systems with instantaneous average-current-sharing scheme", *IEEE Trans. Power Electron*, Vol. 18, No. 3, May 2003, pp. 844-856.

[14] C.-L. Chen, Y. Wang, J.-S. Lai, Y.-S. Lee, and D. Martin, "Design of parallel inverters for smooth mode transfer microgrid applications", *IEEE Trans. Power Electron*, Vol. 25, No. 1, Jan. 2010, pp. 615.

[15] T.-F. Wu, Y.-K. Chen, and Y.-H. Huang, "3C strategy for inverters in parallel operation achieving an equal current distribution", *IEEE Trans. Ind. Electron.*, Vol. 47, No. 2, Apr. 2000, pp. 273-281.

[16] R. Majumder, B. Chaudhuri, A. Ghosh, R. Majumder, G. Ledwich, and F. Zare, "Improvement of stability and load sharing in an autonomous microgrid using supplementary droop control loop", *IEEE Trans. Power Syst.*, Vol. 25, No. 2, May 2010, pp. 796-808.

[17] M. Prodanovic and T. C. Green, "High-quality power generation through distributed control of a power park microgrid", *IEEE Trans. Ind. Electron.*, Vol. 53, No. 5, Oct. 2006, pp. 1471-1482.

[18] Y. Arya, "A new optimized fuzzy FOPI-FOPD controller for automatic generation control of electric power systems", *Journal of the Franklin Institute*, Vol. 356, No. 11, Nov. 2019, pp. 5611-5629.

[19] D. C. Freitas, A. M. N. Lima, and M. R. A. Morais, "Determining Lead-Acid Battery DC Resistance by Tremblay Battery Model", *7th International Renewable Energy Congress* (IREC), 22-24 Mar. 2016, pp. 1-4.

[20] A. Abd El, E. Bayoumi, W. El-Khattam, and A. Ibrahim, "Effect of fast charging on lithium ion batteries: A review", *SAE International Journal of Electrified Vehicles*, Vol. 12, No. 3, 2023, pp: 361-388. https://doi.org/10.4271/14-12-03-0018.

[21] K. Subramanian, and N, S. "An Off-board Electric Vehicle Battery Charger using PV Array", *IET Electrical Systems in Transportation*, Vol. 10, No. 3, 2020, pp. 291-300, doi: 10.1049/iet-est.2019.0035.

[22] Zhong, C., Li, G., Meng, Z., Li, H., Yildiz, A. R., and Mirjalili, S. "Starfish optimization algorithm (sfoa): a bio-inspired metaheuristic algorithm for global optimization compared with 100 optimizers", *Neural Computing and Applications*, Vol. 37, No. 5, 2025, pp. 3641–3683.

[23] Jayasree. K and Malaya K. Hota "SFOA-based optimized SeResNet-BiLSTM network with an attention mechanism for the detection of exons" BMC Genomics, July 2026, https://doi.org/10.1186/s12864-026-13194-9.

Contribution of Individual Authors to the Creation of a Scientific Article (Ghostwriting Policy)

The authors equally contributed in the present research, at all stages from the formulation of the problem to the final findings and solution.

Sources of Funding for Research Presented in a Scientific Article or Scientific Article Itself

No funding was received for conducting this study.

Conflict of Interest

The authors have no conflicts of interest to declare that are relevant to the content of this article.

Creative Commons Attribution License 4.0 (Attribution 4.0 International, CC BY 4.0)

This article is published under the terms of the Creative Commons Attribution License 4.0
https://creativecommons.org/licenses/by/4.0/deed.en_US

APPENDIX

Table A1. PV parameters

Parameter	Symbol	Value
Array Data		
Parallel Strings		25 deg
Series -Connected modules per String		12
Module Data		
Input 1= Sun Irradiance in W/m2		
Input 1= Cell Temperature in deg.c		
Module= SunPower SPR-305E-WHT-D		
Maximum Power	Pmax	305.226 W
Cell Per Module	Ncell	96
Open Circuit Voltage	Voc	64.2 V
Short Circuit Current	Isc	5.96 A
Voltage at Maximum Power Point	Vmp	54.7 W
Current at Maximum Power Point	Imp	5.58 A
Temperature Coefficient of Voc(%/deg.c)	Voc% /T	-0.2727 %/deg.c
Temperature Coefficient of Ioc(%/deg.c)	Ioc%/T	0.061745 %/deg.c
Model		
Light-generated Current	IL	5.9657 A
Diode Saturation Current	IO	6.3076e-12 A
Shunt Resistance	Rsh	393.2054 Ω
Series Resistance	Rs	0.37428 Ω
Irradiances	Irr	1000 W/m2
Phase Locked Loop		
Minimum Frequency	F	0.75*50
Phase	wt	0 deg
Frequency	F	50 HZ
Regulator Gain	Kp	60
Regulator Gain	Ki	1400
Time Constant for Derivative action	TcD	1e-4 Sec
Maximum rate of change of Frequency	F	12 HZ/Sec
Filter cut-off Frequency for Frequency measurement	F	25 HZ
Positive Sequence (PLL-Driven)		
Initial Frequency	Fin	50 HZ
Minimum Frequency	Fmin	0.75*50

Source: created by the authors

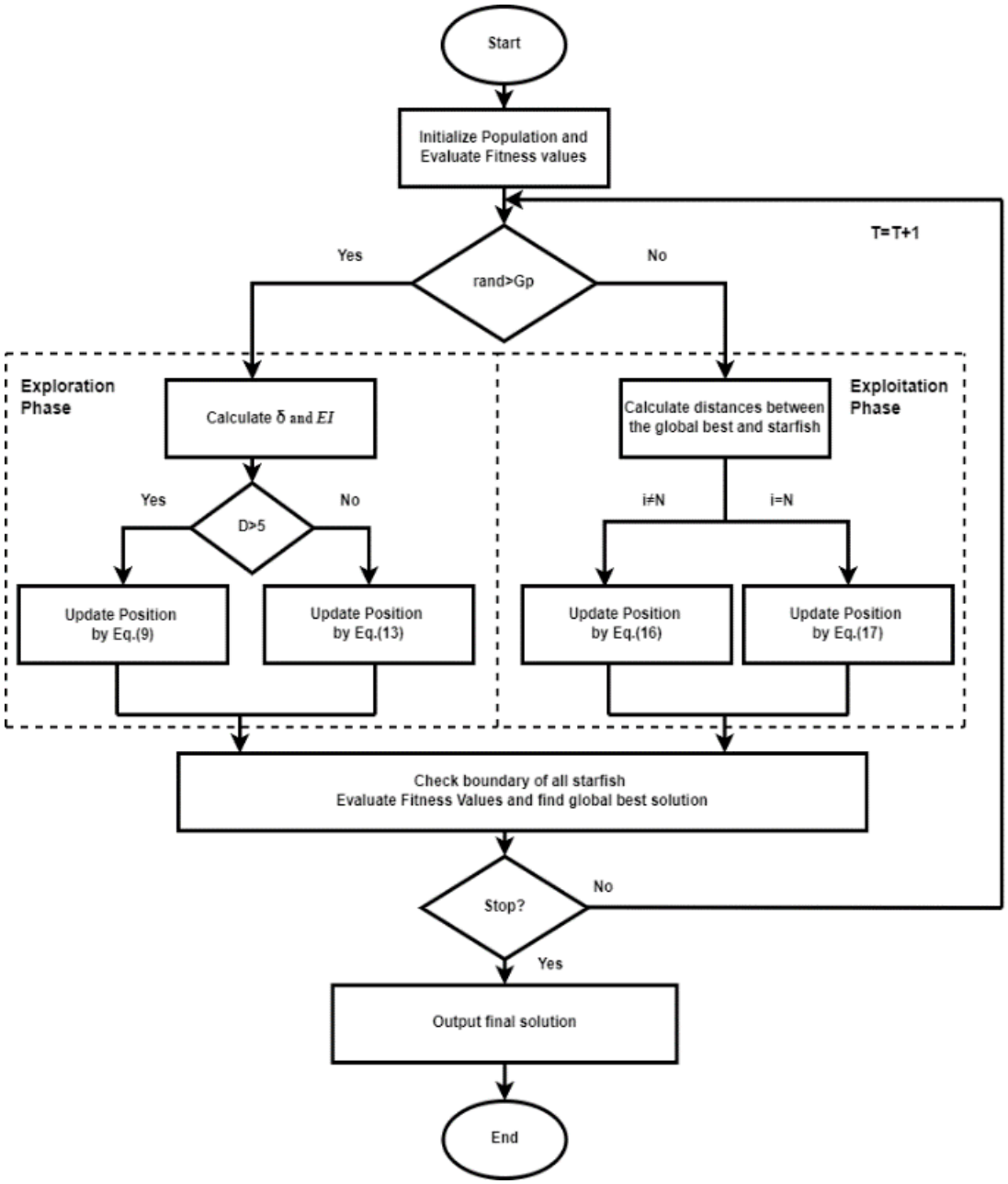


Fig. 14: The flowcharts of SFOA
Source: [23]